# Spin-dependent charge state interconversion of nitrogen vacancy centers in nanodiamonds

Reece P. Roberts,[1,2] Mathieu L. Juan,[3] and Gabriel Molina-Terriza[4,5]

[1]*Department of Physics and Astronomy, Macquarie University, NSW 2109 Sydney, Australia*

[2]*ARC Centre for Engineered Quantum Systems, Macquarie University, NSW 2109 Sydney, Australia*

[3]*Institute for Quantum Optics and Quantum Information of the Austrian Academy of Sciences, 6020 Innsbruck, Austria*

[4]*Centro de Física de Materiales de San Sebastián, CFM-MPC (CSIC-UPV/EHU), Paseo Manuel Lardizabal 5, 20018 Donostia-San Sebastián, Spain*

[5]*Donostia International Physics Center, 20018 Donostia-San Sebastián, Spain*

(Received 27 June 2018; revised manuscript received 22 January 2019; published 17 May 2019)

The nitrogen vacancy (NV) center in diamond is the most widely studied color center in diamond for its wide range of applications in both physics and biology. The negatively charged state $NV^-$ is often favored for its better spin-optical properties, whereas the presence of the neutral charge state $NV^0$ is often minimized or neglected by using a single optimized excitation wavelength. In many cases, the use of additional laser wavelengths has an important impact on the NV optical properties and can lead to a dramatically quenched fluorescence. Through measurements of the photophysics of the NV center we show in this work that this quenching mechanism is mediated by charge state interconversion providing additional channels for nonradiative decay. Our results show that this mechanism is also sensitive to the spin state of the $NV^-$. A better understanding of this physical mechanism will help mitigate the spin and charge state depolarization effects that are detrimental for quantum technology applications.

DOI: 10.1103/PhysRevB.99.174307

## I. INTRODUCTION

The most widely studied color center in diamond, the nitrogen vacancy (NV) center, is a point defect consisting of a nitrogen vacancy lattice pair embedded along the [111] axis of a diamond [1]. The NV center has two stable charge states, the neutral charge state ($NV^0$) and the negatively charged state ($NV^-$), with photoinduced interconversion between these two states [2]. Of the two charge states, the $NV^-$ has been intensively studied for a wide range of applications in both physics and biology due to its high stability and interesting spin-optical properties [3]. In the context of biology, $NV^-$ has been extensively used for biolabeling and imaging of internal biological structures [4,5]. Meanwhile, physicists have been investigating their use for nanoscale sensing and quantum technology applications [6–11]. By exploiting the defects' internal spin state, quantum effects at room temperature can be observed in the $NV^-$ center, providing a platform to study a wide variety of quantum manipulation protocols [12]. However, these desirable effects rely solely on the properties arising from the $NV^-$ charge state, and in most applications the excitation wavelength is chosen to be from 510 and 540 nm in order to maximize the $NV^-$ charge state polarization [13]. By using a single optimized excitation wavelength the impact of the neutral charge state $NV^0$ is often neglected despite the optimal charge state polarization being limited at $\approx$75% [13]. While the spin-optical properties of NV centers are extremely robust [14], this is dependent on the ability to maintain the $NV^-$ charge polarization. It has been observed, however, that once a second probe laser is used in an experiment, the fluorescence of the NV center can be dramatically quenched [4,15–18]. This quenching has been used for stimulated emission depletion (STED) microscopy in biology, whereas for other applications relying directly on fluorescence the quenching prevents the efficient use of NV centers in systems that require additional laser wavelengths. It is therefore essential to understand the quenching processes induced by the interplay between the charge states in the NV center when using more than one wavelength.

In this work we clarify some of the mechanisms which lead to the quenching of the NV center fluorescence. We find that this quenching is driven by a continuous charge state transfer between $NV^0$ and $NV^-$ providing increased channels for nonradiative decay from the excited states. In addition, we show that the ionization from the $NV^-$ to $NV^0$ charge state strongly depends on the spin state of the $NV^-$. Having a better understanding of this mechanism is essential for any application that requires a spin manipulation protocol. We experimentally observe the charge state interconversion process by probing the NV centers with a near-infrared (NIR) laser. In order to avoid fast dynamics and nonlinear effects [15–17], we choose to use a 785-nm continuous-wave NIR laser with only a few tens of milliwatts. This steady-state regime is particularly interesting for applications relying on fluorescence, optical forces [19], and optical levitation [20,21]. Then, we collect the fluorescence of both charge states and show that the impact of the $NV^0$ charge state cannot be neglected in a steady state regime.

## II. METHODS

### A. Experiment

In our experiment, 100-nm-diameter nanodiamonds are dispersed on a glass coverslip placed on the sample plane of a custom-built scanning confocal microscope. We used

 

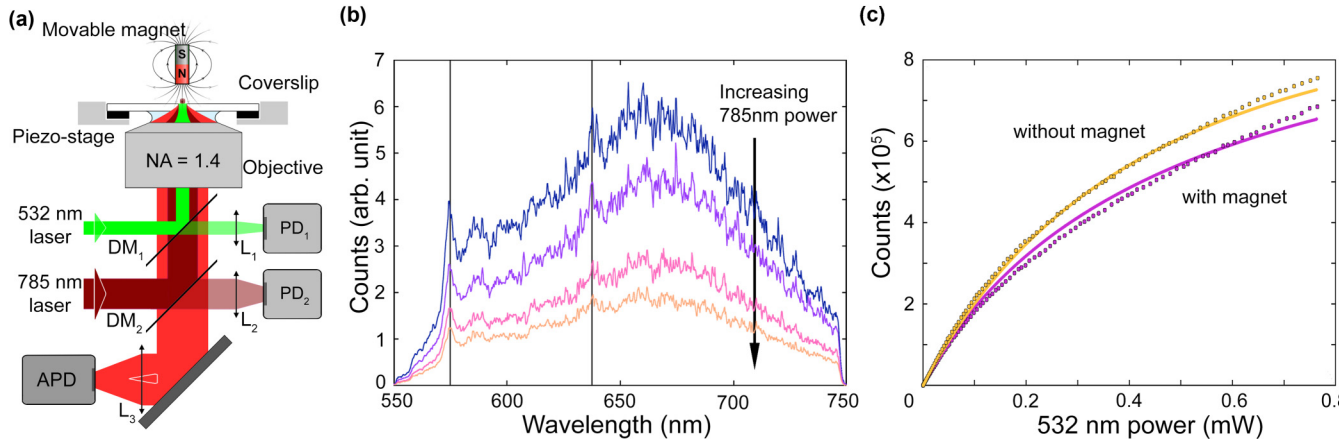


FIG. 1. Experimental approach. (a) Schematic of the experimental setup where the nanodiamond, deposited on a coverslip, is positioned using a piezo stage. The two incident lasers (532 and 785 nm) are combined using two dichroic mirrors ($DM_1$ and $DM_2$) and focused by the 1.4 numerical aperture objective. The small portion of the incident power that is transmitted through the dichroic mirrors is used to monitor the power of each laser using photodiodes (PDs). The emission from the nanodiamond is collected by the same objective and sent through the dichroic mirrors and a filter to an avalanche photodiode (APD). (b) Spectrum recorded for 0.75 mW of 532 nm for four different 785-nm powers: 0, 2.3, 9.7, and 21 mW in order from dark- to light-colored curves. (c) Saturation curve for a given nanodiamond without and with a magnet in close proximity in light and dark colors, respectively. The open symbols are the experimental measurement, while the curves show the result from the best model obtained by fitting both the saturation curve and the fluorescence quenching presented in Fig. 2.

synthetic type Ib nanodiamonds irradiated by a 3 MeV proton beam at a dose of $10^6$ ions per $cm^2$ and annealed in vacuum at 700 °C for 2 h to obtain a high density of NV centers (∼30 ppm), providing high brightness useful for biological applications and sensing [22]. The NV centers are excited with a 532-nm continuous-wave laser using a 1.4 numerical aperture objective. The 785-nm NIR laser is combined and superimposed with the 532-nm laser before the objective lens, so the two foci are overlapping in the sample plane. The fluorescence is back collected through the same objective and sent to either a fibered spectrometer or a fibered coupled avalanche photodiode (APD) collecting all wavelengths from 550 and 750 nm. A permanent neodymium magnet is placed on a movable arm above the sample plane so that a large nonzero magnetic field could be brought in close proximity to the nanodiamond. The effect of the magnet is to mix the internal spin state of the $NV^-$ which can be observed through a reduction in fluorescence signal [23]. The setup is shown in Fig. 1(a).

We first examined the spectral response of excited NV centers under NIR illumination in a spectral window from 550 and 750 nm showing both the $NV^0$ and the $NV^-$. We excited the NV centers with a fixed power of 0.75 mW of 532 nm and acquired fluorescence spectra for varying powers of incident NIR [see Fig. 1(b)]. The fluorescences of both $NV^0$ and $NV^-$ can be observed to be decreasing with increased NIR power. This overall quenching of the fluorescence as a function of the incident power of 785 nm is confirmed by the APD measurements. We could not observe any differences on the relative ratio of $NV^0$ to $NV^-$ emissions due to the inability to distinguish precisely the two charge states at room temperature; however, the fact that the whole spectrum is affected by the NIR in the same way indicates that the quenching of fluorescence cannot be explained by simply a change in the charge polarization of the NV center.

In order to investigate the photodynamics of the NV centers in more detail, we used the APD to observe the fluorescence for varied excitation and quenching powers. This allows us to explore a large parameter space for model fitting. For each of the five measured nanodiamonds we retrieved first the saturation curve of the NV centers [see Fig. 1(c)]. The power dependence of the fluorescence for the 785-nm illumination wavelength was then measured for five powers of the 532-nm excitation laser. The measurements were repeated with a neodymium magnet disk (2.5 × 2 $mm^2$, grade N42) placed ≃0.5 mm above the sample plane of the confocal microscope in order to mix the spin state of the $NV^-$ charge state. On axis, the magnet produces a magnetic field of ≃0.43T at the nanodiamond position, leading to an important spin mixing mediated via Zeeman splitting but also due to the large number of spin impurities in our nanodiamonds. This allowed us to study the impact of the spin state of $NV^-$ on the fluorescence quenching. For each nanodiamond we observe similar behavior. Figure 2 shows one of the nanodiamonds characterized as an example.

### B. Model

To determine the intrinsic photophysics of our nanodiamonds we developed a rate equation model with eight levels. This model, described in further detail in Appendix C, incorporates all known mechanisms that could lead to quenching, including the charge state interconversion mechanisms between $NV^0$ and $NV^-$ [2] as well as a STED-like mechanism. Whether the STED-like effect is simply nonradiative decay from the excited to ground triplet state [4] or is mediated through a new fast-decaying dark band [18], the mechanisms reduce to identical rate equations. In order to fit the data we also had to include a spin-state dependence in the charge state interconversion. Our task then is to determine the mechanisms dominating in the fluorescence quenching of NV centers at 785 nm, varying the number of free parameters of the model. In total, we studied five submodels and identified the best

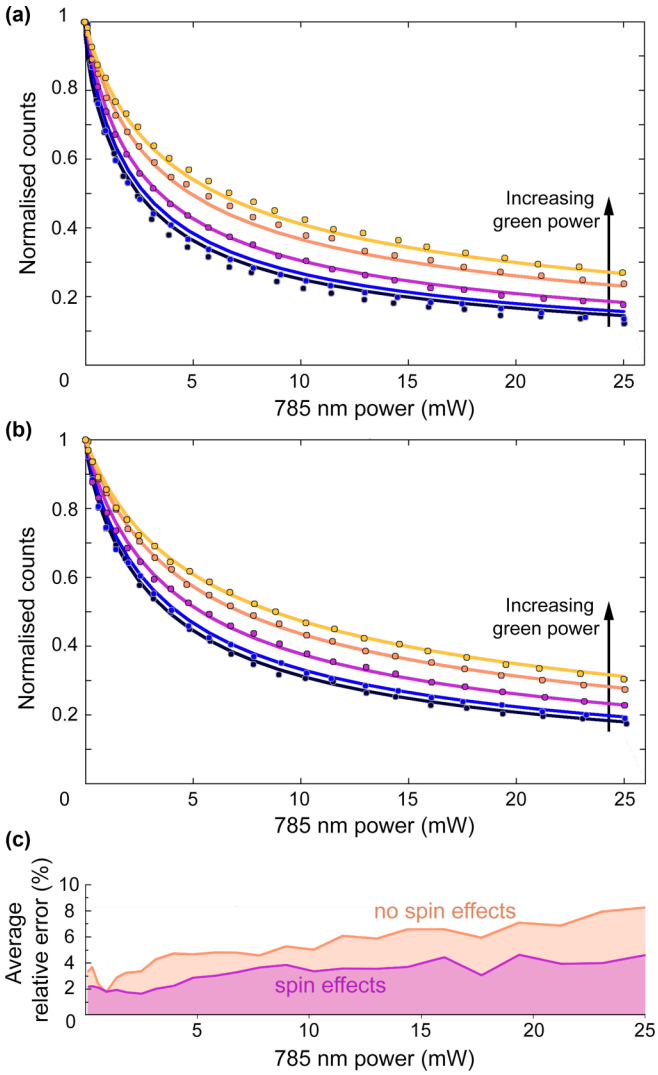


FIG. 2. Experimental data. (a) Fluorescence quenching for a given nanodiamond as a function of the incident near-infrared power. The different curves are obtained for different green powers: 0.03, 0.07, 0.22, 0.5, 0.74, and 0.72 mW from dark- to light-colored curves. (b) Same as (a), with a magnet in close proximity to the nanodiamond. (c) Comparison of the average relative error between the fit and the experimental fluorescence quenching when accounting or not for a spin-dependent ionization in the model.

model for our data using the Akaike information criterion [24]. We discuss here only the most likely model; however, the full analysis of all the potential models and the theory for the charge state interconversion processes are discussed in Appendixes C and B, respectively. The model, identified by the Akaike information criterion as being 3 times more likely than the next best model (Appendix D), indicates that the quenching process occurs through continuous charge state transfer between $NV^0$ and $NV^-$, leading to increased nonradiative decay through charge state interconversion of the NV center without any significant STED-like process. It is important to note that the STED-like mechanism alone could not account for the effects of the internal spin dynamics identified by applying the magnet. Comparing the models using the Akaike information criterion confirms that the

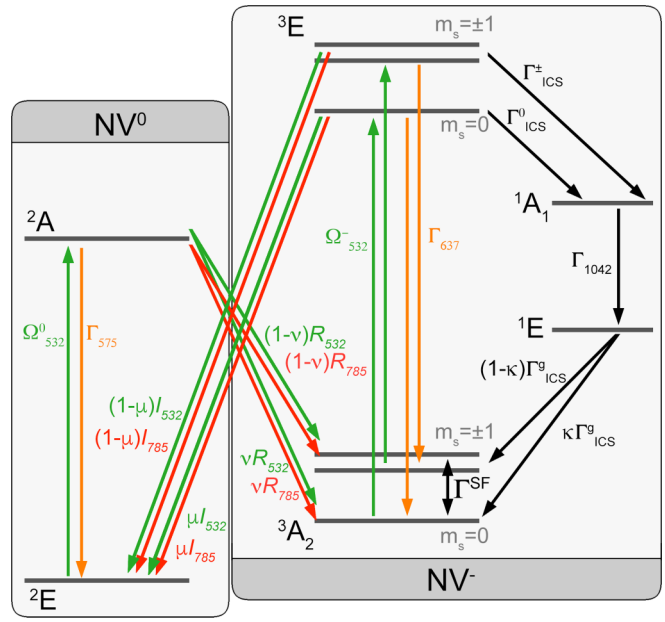


FIG. 3. Energy levels of both charge states of the NV center.

steady state photophysics of the NV center is not significantly impacted by having an additional STED-like process. We note, however, that this process may be relevant in time-resolved measurements. Also, we did not account for direct electric and magnetic interactions between NV centers, which could impact the fluorescence quenching, due to the numerical complexity of this problem [25].

The energy level structure and fitting parameters for the processes leading to the quenching observed through the charge state interconversion processes are shown in Fig. 3. While the model is kept quite general and the free parameters are unconstrained, the final values are physically meaningful and comparable with measurements reported in the literature. For the fixed parameters, we used well-established values from the literature (Appendix A). In addition, to account for the modification of the lifetime of $NV^0$ centers in nanodiamonds due to local field effects, we used an average lifetime of 26 ns instead of the usual 13 ns in bulk [26,27]. The final model parameters are given in Table I. We observe two types of model free parameters, those that are dependent on the

TABLE I. Final model parameters. The spin mixing in the ground state $\Gamma^{SF}$ is denoted $\Gamma^{SF}_{NoMag}$ in the absence of the magnet and $\Gamma^{SF}_{Mag}$ when the magnet is present.

| Fixed parameters | Free parameters |
|---|---|
| $\Gamma_{1042} = 1$ GHz [28] | $\Omega^{-}_{532} = 28 \pm 0.8$ MHz mW$^{-1}$ |
| $\Gamma^{g}_{ICS} = 6.6$ MHz [29] | $\Gamma^{SF}_{Mag} = 6.2 \pm 3.7$ MHz |
| $\Gamma^{\pm}_{ICS} = 59$ MHz [30,31] | $\kappa = 0.70 \pm 0.23$ |
| $\Gamma^{0}_{ICS} = 11$ MHz [30,31] | $I_{532} = 14.3 \pm 6.3$ MHz mW$^{-1}$ |
| $\Gamma_{637} = 38$ MHz [26] | $I_{785} = 9.40 \pm 0.50$ MHz mW$^{-1}$ |
| $\Gamma_{575} = 26$ MHz [32] | $\mu = 0.837 \pm 0.005$ |
| $\Omega^{0}_{532} = \frac{1}{3}\Omega^{-}_{532}$ [13,33] | $R_{532} = 182 \pm 91$ MHz mW$^{-1}$ |
| $\Gamma^{SF}_{NoMag} = 1$ KHz [34] | $R_{785} = 18.8 \pm 1.8$ MHz mW$^{-1}$ |
| | $\nu = 0.49 \pm 0.06$ |

internal NV structure and those that are influenced by the nanodiamond structure, i.e., strain or surface effects. When we consider the values that are related to the internal NV structure of the nanodiamond, the results obtained from the model are more consistent between different nanodiamonds.

## III. DISCUSSION

The model shows that under strong NIR illumination, the continuous charge state interconversion processes provide a nonradiative decay across the different charge states: the ionization (recombination) provides a path from the excited state of the $NV^-$ ($NV^0$) to the ground state of the $NV^0$ ($NV^-$). Under steady-state conditions the ionization and recombination driving rates for the 532-nm laser are consistent with the charge state transfer rates for single NV centers in nanodiamonds [13]. Such driving between charge states is then dramatically increased by the addition of the 785-nm NIR laser. We note that it is difficult to directly compare the ionization and recombination rates between the two laser wavelengths as the photodynamics are different for each wavelength. The 785-nm laser cannot ionize/recombine the NV centers without the additional excitation of the transition provided by the 532-nm laser. The main result of our model is that as soon as the incident NIR power exceeds a few milliwatts the ionization/recombination rate is comparable to or larger than the spontaneous decay rates of the NV center. This process is sufficient to explain the observed fluorescence quenching. Furthermore, by obtaining measurements with a magnet to mix the $NV^-$ ground state spin, we could also study the spin dependence of such ionization/recombination processes. The exact value of the spin mixing, $\Gamma^{SF}_{Mag} = (6.2 \pm 3.4)$ MHz, depends strongly on the exact spatial distribution of NV centers and neighboring spin impurities within the diamond crystal and, consequently, varies between nanodiamonds. We note that the spin mixing due to the external magnetic field is a combination of several effects that have been accounted for with one phenomenological spin-mixing rate. The spin dynamics we obtained for the $NV^-$ through the singlet state closely matches the values reported in the literature where the recombination to the $NV^-$ ground state favors the $m_s = 0$ state over the $m_s = \pm 1$ states but varies significantly between nanodiamonds ($\kappa = 0.70 \pm 0.23$) [29,35]. In addition we can verify, using the rate equations (C2), that in the absence of driving lasers (532 and 785 nm) our model predicts a spin polarization of zero.

Interestingly, the model also indicates that the $NV^- \rightarrow NV^0$ ionization process is a spin-dependent process. On a phenomenological level, this effect is similar to the spin dependent charge dynamics under 1064 nm laser excitation [36] but has important consequence on the spin state of the $NV^-$. In the work of Jelezko, Warchtrup, and colleagues [2] it was proposed that this process involves two photons and an Auger ionization process. This mechanism was also recently used to explain the charge dynamics of shallow NVs [37]. Our results suggest that in addition this Auger process is spin dependent, significantly favoring ionization from the $m_s = 0$ spin state. This is clearly visible when comparing the relative error of fits from the models with and without this spin-dependent ionization process [see Fig. 2(c)]. Using the Akaike information criterion, the Akaike weight for the model without spin dependence is negligible relative to the model with spin dependence, confirming that this effect needs to be taken into account to properly describe our experimental data. Remarkably, the spin selectivity of the ionization process is the same between nanodiamonds with a very small variation of the $\mu$ coefficient for the different nanodiamonds measured ($\mu = 0.837 \pm 0.005$). This is consistent with a process related to the photophysical properties of the $NV^-$ center with little to no effect from any of the neighboring impurities in the crystal. One important consequence of this spin selectivity is the impact of the 785-nm laser on the spin polarization of the $NV^-$. For example, when operating above saturation (532-nm power of $\sim$1 mW), moderate powers of 785 nm do not appreciably change the charge state since the 532-nm will efficiently polarize the NV into $NV^-$. On the other hand, the spin polarization is significantly modified, as can be seen in Fig. 4. In most quantum applications of NV centers, the control of the spin plays a central role. In particular, the spin initialization is typically realized using 532-nm pumping to efficiently prepare the $NV^-$ in the $m_s = 0$ spin state. Our results show that even a moderate amount of 785 nm is sufficient to significantly reduce the spin polarization. As a result under NIR illumination the charge state interconversion process must be taken into account in order to prepare the charge state of the NV and also for

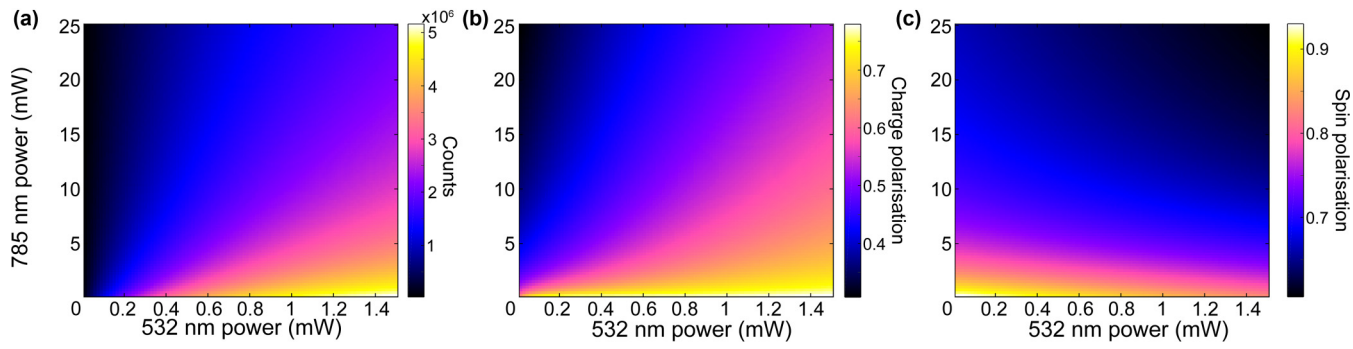


FIG. 4. Predicted fluorescence, charge polarization, and spin polarization. (a) Fluorescence count, (b) charge polarization (1 is completely in the $NV^-$ state), and (c) spin polarization (1 is completely in the $m_s = 0$ state) obtained using our model with the average parameters obtained from fitting the experimental measurements from five distinct nanodiamonds. While for very low 532-nm laser power the spin state should thermalize, the lowest power used here is sufficient to overcome this spin relaxation effect.

preparation of the spin state of the $NV^-$ for quantum manipulation protocols.

For high-resolution microscopy in which this process is used, maximizing the quenching power would increase the resolution of the imaging. In order to maximize the STED-like effect, the quenching laser would ideally be one that maximizes the ionization and recombination rates. The ionization and recombination quenching process could be dramatically increased by first exciting each charge state at the zero-phonon line (ZPL) and further driving the ionization and recombination process with an additional quenching laser. Identifying the optimal driving laser wavelength can be determined by observing the quenching of a nanodiamond as a function of quenching laser wavelength. This result is consistent with the work of Sun and colleagues [38]. Finally, in comparison to traditional STED microscopy, this charge state interconversion microscopy uses more laser wavelengths for imaging but reduces total laser power incident on the sample, reducing the heating and photodamage of the sample.

These results show that the NIR illumination plays a critical role on the photodynamics of the NV center which could have a detrimental effect on manipulation protocols of the quantum state of the $NV^-$ center. A logical next step towards understanding and controlling the charge state interconversion processes is to investigate the wavelength dependence and the effect of the local environment on these processes. For example, the strain on the crystal and density of nitrogen in the crystal could significantly impact the ionization and recombination rates. In addition, by capitalizing on the various timescales of the processes at play we believe it will be possible to achieve a better control on either the charge state or the spin state of the NV centers by pulse sequencing the different lasers wavelengths. Furthermore, it would be interesting to include collective effects between NV centers [25] as they would increase the radiative emission rate of the NV, potentially mitigating quenching effects.

## ACKNOWLEDGMENTS

This work was funded by the Australian Research Council's Centre of Excellence for Engineered Quantum Systems (EQuS) and the Australian Research Council Future Fellowship program (Grant No. FT11010092).

## APPENDIX A: NV STRUCTURE

### 1. $NV^-$ Structure

The $NV^-$ charge state consists of a ground triplet state $^3A_2$ and an excited triplet state $^3E$, as well as two metastable singlet states, $^1E_1$ and $^1A_1$ [3]. Within the spin triplet states the $m_s = 0$ and $m_s = \pm 1$ spin states are split in energy at zero magnetic field by $D = 2.87$ GHz for the ground triplet and $D = 1.42$ GHz for the excited triplet [3]. The spin transition rate between the ground $m_s = 0$ and $m_s = \pm 1$ spin states is given by the spin-lattice relaxation time $T_1$ and has been measured to be $\Gamma^{\mathrm{SF}} \approx 6$ ms $= 167$ Hz at room temperature and zero magnetic field [34]. This spin-mixing rate can be dramatically increased by applying a large magnetic field in the vicinity of the NV center.

The principle zero-phonon line between $^3A_2$ and $^3E$ is centered at 637 nm and can be efficiently excited with spin conservation at most wavelengths below 640 nm [3]. The radiative lifetime of the excited state is 13 ns for NV centers in bulk diamond and approximately 25 ns for NV centers in nanodiamonds [26,27]. Only a few percent of the fluorescence are emitted at the ZPL; most fluorescence appears in the phonon sidebands between 600 and 800 nm.

The excited triplet states can also decay to the excited singlet state; the rate from the $m_s = \pm 1$ excited triplet state is $\Gamma^{\pm}_{\mathrm{ICS}} = 2\pi \times 9.4\,\mathrm{MHz} = 16.9$ ns, whereas the rate from the $m_s = 0$ excited triplet state is almost an order of magnitude smaller at $\Gamma^{0}_{\mathrm{ICS}} = 2\pi \times 1.8\,\mathrm{MHz} = 88.4$ ns [30,31]. While it is not completely understood why there is a large discrepancy between these decay channels, it is noteworthy that this discrepancy enables many of the interesting optical properties of the NV center. It leads to the difference in fluorescence intensity between the two excited spin states, which in turn leads to a mechanism for an all-optical readout of the center's internal spin state. The excited singlet state has a lifetime of $\Gamma_{1042} \approx 1$ ns [28] populating the longer-lived ground singlet state, and it has been shown to emit fluorescence at a ZPL of 1042 nm [28,39]. The longer-lived ground metastable state has a lifetime of $\Gamma^{g}_{\mathrm{ICS}} \approx 150$ ns and decays into the ground state from the triplet spin state [28]. It was commonly believed that this population decayed only into the $m_s = 0$ spin state; however, recently, this was challenged, and it has been claimed that the decay into the ground triplet is nanodiamond dependent and only $\kappa = 0.5$–$0.7$ of the electrons decay into the $m_s = 0$ ground state [29,35].

### 2. $NV^0$ Structure

As opposed to the rigorous study the $NV^-$ charge state has received, the $NV^0$ charge state has often been neglected. However, we believe in order to study the NV center as a whole it must be included. We use the established three-level model to describe its intrinsic dynamics. The $NV^0$ charge state consists of a ground doublet $^2E$ and an excited doublet $^2A$ with a ZPL at 575 nm $= 2.156$ eV [3]. It can be efficiently excited at most wavelengths below 675 nm and in bulk diamonds has a radiative lifetime of $\Gamma_{575} = 19$ ns [32,40]. In nanodiamonds, the radiative lifetime is altered due to the changed phonon density of states due to the size of the nanodiamonds. Since the wavelengths of the emission for $NV^0$ and $NV^-$ are similar, it is expected that the $NV^0$ radiative lifetime will increase by approximately the same factor as $NV^-$ in nanodiamonds compared to bulk diamond, and as such the radiative lifetime set for the model was $\Gamma_{575} = 38$ ns [26,27]. The exact excitation cross section of the $NV^0$ center is unknown; however, the ratio of excitation cross sections between $NV^0$ and $NV^-$ can be measured by looking at their relative emission intensities. Since the quantum efficiency of both $NV^0$ and $NV^-$ is $\approx 1$, the ratio of excitation cross sections is given by the ratio of emission cross sections, giving $\Omega^{0}_{532} = \frac{1}{3}\Omega^{-}_{532}$ [13,33]. Differing from $NV^-$, $NV^0$ does not have detectable magnetic resonances associated with its degenerate spin doublet ground and excited states [41]. Only a few percent of the fluorescence are emitted in the ZPL, whereas most fluorescence appears in the phonon sidebands between 550 and 750 nm. The third

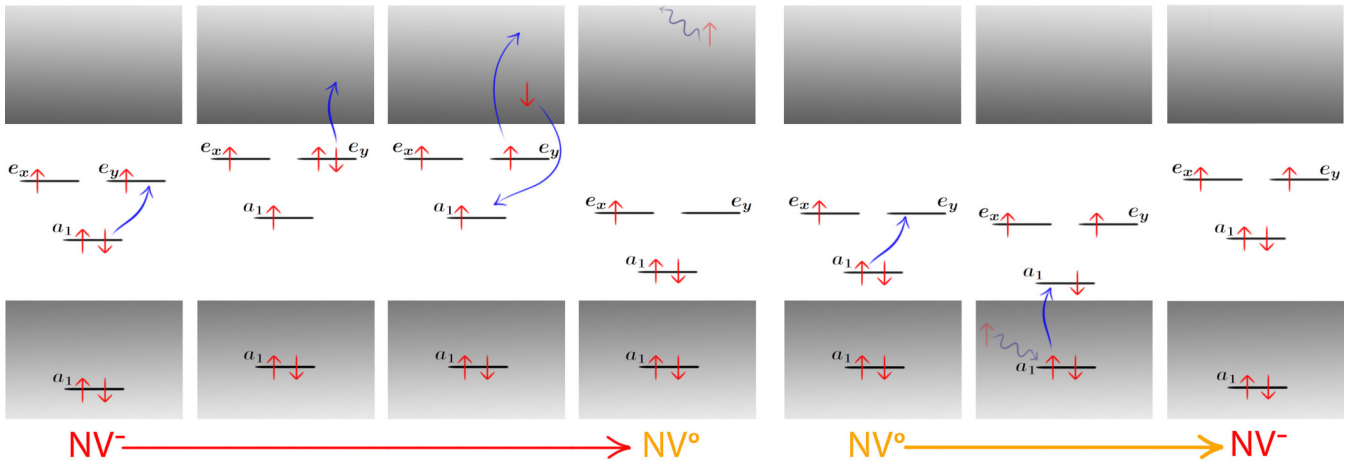


FIG. 5. Ionization and recombination processes. Schematic of the internal electron orbital structure for the NV charge conversion process between the negative and neutral charge states of the NV center. The NV center is in the $NV^0$ charge state when there are five electrons in the structure and in the $NV^-$ center when there is an extra sixth electron in the structure. The $NV^-$ to $NV^0$ conversion involves two-photon excitation followed by an Auger process that releases enough energy to ionize an electron from the structure, leaving the defect in the ground state of the $NV^0$. The recombination process from $NV^0$ to $NV^-$ is also a two-step process. First, the neutral defect is excited, as shown by the movement of an electron from the $a_1$ orbital to the $e$ orbital. Before decay can occur an additional electron is transferred from the $a_1$ orbital in the valence band to the vacant place on the $a_1$ orbital in the band gap. The vacant place in the deep-lying $a_1$ orbital is then replaced by a new electron from the valance band leaving the center in the ground state of the $NV^-$. The positions of orbital levels change with different electron configurations throughout both processes. The energy level labels in this diagram arise from a group theory representation of the internal orbital structure and are different from the typical energy level diagrams that are shown for the NV center.

energy level attributed to the $NV^0$ is the metastable spin quartet $^4A_2$, which was measured through an electronic parametric signal [41]. However, no optically detected magnetic resonance or optical readout of this metastable quartet has been measured, and it is expected to have a negligible impact on the photophysics of the NV center and, as such, has been neglected from our analysis.

## APPENDIX B: CHARGE STATE CONVERSION

To convert between the two charge states we need to examine both the ionization process from $NV^-$ to $NV^0$ and the recombination process from $NV^0$ to $NV^-$. The desirable effects of the NV center rely solely on the properties arising from the $NV^-$ charge state, and as a result a standard ≈532-nm excitation laser used in NV center applications is chosen so that it produces the highest charge state polarization in an effort to optimize the effect and allow any effects due to the $NV^0$ charge state to be neglected [13]. However, we believe that not only will the excitation laser alter this balance but any additional laser is going to alter this maximized charge state polarization under continuous-wave excitation.

### 1. Ionization

Ionization from $NV^-$ to $NV^0$ occurs in a two-step process, as shown in Fig. 5.

First, a photon must excite an electron into the excited $^3E$ state of the $NV^-$. The electron can then be excited again into the conduction band, leading to an Auger ionization process which strips an electron from the center, converting it into the $NV^0$ charge state in its ground state configuration [2]. This two-step process has been investigated only with a single-excitation laser, which leads to an ionization rate that is quadratic with excitation power and can no longer occur at wavelengths greater than the ZPL of the transition. However, we observe that this process can be mediated by two lasers, one that strongly excites the transition and one that strongly ionizes the electron leading to the Auger ionization process. One would initially assume that the ionization mechanism would be spin independent; however, these energy levels already show a spin-dependent nature towards the singlet states that leads to the spin polarization properties of the $NV^-$. Additionally, spin-dependent charge state interconversion was previously observed [36]. Since the dipole strengths of the two excited spin states differ by an order of magnitude, the symmetry of the Auger ionization process can break, leading to different ionization rates for each excited spin state. As a result we investigated the possibility that the interactional cross sections of the excited $NV^-$ center can be spin dependent.

### 2. Recombination

The recombination process from $NV^0$ to $NV^-$ also occurs in a two-step process and is shown in Fig. 5. First, a photon must excite an electron in the $NV^0$ charge state into the excited $^2A$ state. A second photon can then be excited from the valence band into the $^2E$ ground state, which provides the extra electron to the center, converting it into the $NV^-$ charge state in its ground state configuration [2]. Currently, there is no evidence to indicate which spin state the $NV^-$ charge state will now be populated in; however, it was recently observed that the recombination process is a spin-depolarizing process, indicating a non-negligible component in the $m_s = \pm 1$ spin state [36]. In our analysis we observe that the rate of recombination from $NV^0$ to $NV^-$ is $180 \pm 90$ MHz/mW at 532 nm and $18 \pm 2$ MHz/mW at 785 nm. Additionally, the

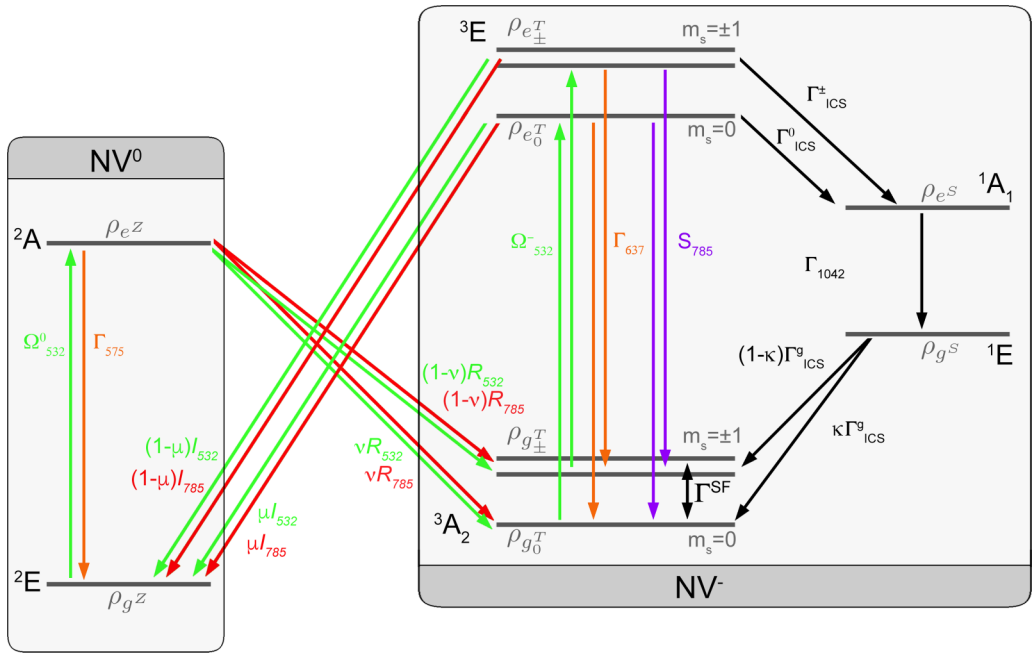


FIG. 6. Energy levels of both charge states of the NV center showing all the stimulated, spontaneous, and nonradiative processes. The black arrows indicate dominantly nonradiative processes, the orange arrows indicate spontaneous emission processes, and the red (785 nm) and green (532 nm) arrows indicate processes that can be stimulated by the corresponding laser wavelength.

model indicates that this process is spin depolarizing such that the ratio into the $m_s = 0$ ground state of the $NV^0$ is 49.0% ± 6% for both laser wavelengths.

It has been proposed that the conversion from $NV^0$ to $NV^-$ is mediated by ionization of single substitutional nitrogen impurities $N_s$ in the nanodiamonds, providing free electrons to combine with the $NV^0$ charge state [41]. Our nanodiamonds are a highly irradiated sample and therefore contain a high concentration of single substitutional nitrogen $N_s$, leading to high rates of recombination due to the 785-nm NIR laser which may not be observed in bulk diamonds on samples with low nitrogen impurities.

## APPENDIX C: MODEL OF THE PHOTOPHYSICS

In order to develop the steady-state equations to describe the photophysics of the system as a whole we needed to determine the key variables that influence the system. The main question is to determine whether the STED-like quenching mechanism itself can explain all of the photodynamics of the system or if it is necessary to include the ionization and recombination mechanisms. In each of these processes we also need to keep track of the internal spin state of the NV center. While all the processes between the two triplet states are spin conserving, it is unclear in which spin state the ground spin state will be when transitioning from either the $NV^0$ charge state or the singlet state, and as such, these have been made free parameters of the model.

From the known dynamics of the system, we developed an energy level diagram that includes the potential transition mechanisms between each state which is shown in Fig. 6. Our model is conceptually similar to that of Meirzada *et al.* [37]; however, we probe the internal spin dynamics of the system by limiting our assumptions of the underlying physics, revealing a strong spin-dependent ionization process. From this energy diagram we developed an eight-level rate equation model that incorporates both the ionization and recombination mechanisms as well as the STED-like mechanisms with a power-dependent rate $S_{785}$. The population change of each energy level is given by

$$
\begin{aligned}
\dot{\rho_{e_0^T}} &= -\rho e_0^T\left(\Gamma_{637} + \Gamma^0_{\mathrm{ICS}} + \mu I_{785}\times\mathcal{P}_{785} + \mu I_{532}\times\mathcal{P}_{532} + \mathrm{S}_{785}\times\mathcal{P}_{785}\right) + \rho_{g_0^T}(\Omega^-_{532}\times\mathcal{P}_{532}),\\
\dot{\rho_{e_\pm^T}} &= -\rho e_\pm^T[\Gamma_{637} + \Gamma^\pm_{\mathrm{ICS}} + (1-\mu)I_{785}\times\mathcal{P}_{785} + (1-\mu)I_{532}\times\mathcal{P}_{532} + \mathrm{S}_{785}\times\mathcal{P}_{785}] + \rho_{g_\pm^T}(\Omega^-_{532}\times\mathcal{P}_{532}),\\
\dot{\rho_{g_0^T}} &= \rho_{e_0^T}(\Gamma_{637}) + \rho_{g^S}\left(\kappa\Gamma^g_{\mathrm{ICS}}\right) + \Gamma^{\mathrm{SF}}\left(\rho_{g_\pm^T} - \rho_{g_0^T}\right) - \rho_{g_0^T}(\Omega^-_{532}\times\mathcal{P}_{532}) + \rho_{e^Z}(\nu R_{532} + \nu R_{785}) + \rho_{e_0^T}(\mathrm{S}_{785}\times\mathcal{P}_{785}),\\
\dot{\rho_{g_\pm^T}} &= \rho_{e_\pm^T}(\Gamma_{637}) + \rho_{g^S}\left[(1-\kappa)\Gamma^g_{\mathrm{ICS}}\right] + \Gamma^{\mathrm{SF}}\left(\rho_{g_0^T} - \rho_{g_\pm^T}\right) - \rho_{g_\pm^T}(\Omega^-_{532}\times\mathcal{P}_{532}) + \rho_{e^Z}[(1-\nu)R_{532} + (1-\nu)R_{785}]\\
&\quad + \rho e_\pm^T(\mathrm{S}_{785}\times\mathcal{P}_{785}),\\
\dot{\rho_{e^S}} &= \rho_{e_0^T}\left(\Gamma^0_{\mathrm{ICS}}\right) + \rho_{e_\pm^T}(\Gamma^\pm_{\mathrm{ICS}}) - \rho_{e^S}(\Gamma_{1042}), \quad \dot{\rho_{g^S}} = \rho_{e^S}(\Gamma_{1042}) - \rho_{g^S}\left(\Gamma^g_{\mathrm{ICS}}\right),\\
\dot{\rho_{e^Z}} &= \rho_{g^Z}\left(\tfrac{1}{3}\Omega^-_{532}\times\mathcal{P}_{532}\right) - \rho_{e^Z}(\Gamma_{575} + R_{532} + R_{785}),\\
\dot{\rho_{g^Z}} &= -\rho_{g^Z}\left(\tfrac{1}{3}\Omega^-_{532}\times\mathcal{P}_{532}\right) + \rho_{e_0^T}(\mu I_{785}\times\mathcal{P}_{785} + \mu I_{532}\times\mathcal{P}_{532}) + \rho_{e_\pm^T}(1-\mu)(I_{785}\times\mathcal{P}_{785} + I_{532}\times\mathcal{P}_{532}).
\end{aligned}
\tag{C1}
$$

The incident power of the 532- and 785-nm lasers are $\mathcal{P}_{532}$ and $\mathcal{P}_{785}$, respectively. The energy level populations can be solved under steady-state conditions, and the fluorescence intensity $F$ is then given by the populations of each of the excited states and their corresponding fluorescence decay rates,

$$F = \Gamma_{637}\left(\rho_{e_\pm^T} + \rho_{e_0^T}\right) + \sigma\Gamma_{575}\rho_{e^Z}, \tag{C2}$$

where $\sigma$ is the ratio between the efficiency of collecting a $NV^-$ photon compared to an $NV^0$ photon, which depends on the fluorescence spectra and the collection window as well as the spectral response of the detector. This was calculated to be $\sigma = 1.5$ for our APD with a fluorescence window between 550 and 750 nm. The fluorescence value is then compared directly against the data for the saturation curves with a single scaling parameter, which is related to the effective number of NV centers and collection efficiency, whereas for the NIR quenching data the data can be compared directly by normalizing to the fluorescence intensity with no NIR laser power,

$$\text{Fluorescence counts (norm.)} = \frac{F(P_{785})}{F(0)}. \tag{C3}$$

From this complete model the free parameters were varied in order to determine the most likely dynamics of the system. Five submodels were investigated, and the most likely model was identified by the Akaike information criterion. The five models are (1) stimulated emission only, (2) spin-independent ionization and recombination, (3) spin-independent ionization and recombination including stimulated emission, (4) spin-dependent ionization and recombination, and (5) spin-dependent ionization and recombination including stimulated emission.

The data were fitted against each model independently, and the free parameters for each model are listed in Tables II–VI. The values denoted with an asterisk are parameters that were fixed for that specific model. Model comparison and selection is detailed in Appendix D. For clarity the units, omitted in the tables, are as follows: $\Omega_{532}^-$, MHz mW$^{-1}$; $I_{532}$, MHz mW$^{-1}$; $I_{785}$, MHz mW$^{-1}$; $R_{532}$, MHz mW$^{-1}$; $R_{785}$, MHz mW$^{-1}$; $S_{785}$, MHz mW$^{-1}$; and $\Gamma_{Mag}^{SF}$, MHz.

TABLE II. Model 1: Results of the fit for each nanodiamond (ND) accounting only for stimulated emission. An asterisk indicates parameters that were fixed for this model.

| | Mean | Standard Deviation | ND1 | ND2 | ND3 | ND4 | ND5 |
|---|---|---|---|---|---|---|---|
| $\Omega_{532}^-$ | 52.6 | 7.6 | 61.2 | 50.4 | 45.4 | 45.7 | 60.1 |
| $\Gamma_{\text{Mag}}^{\text{SF}}$ | 2.5 | 1.1 | 4.2 | 1.4 | 2.8 | 1.5 | 2.7 |
| $\kappa$ | 0.57 | 0.13 | 0.64 | 0.66 | 0.38 | 0.66 | 0.49 |
| $I_{532}$* | – | – | 0 | 0 | 0 | 0 | 0 |
| $I_{785}$* | – | – | 0 | 0 | 0 | 0 | 0 |
| $\mu$* | – | – | 0 | 0 | 0 | 0 | 0 |
| $R_{532}$* | – | – | 1 | 1 | 1 | 1 | 1 |
| $R_{785}$* | – | – | 0 | 0 | 0 | 0 | 0 |
| $\nu$* | – | – | 0 | 0 | 0 | 0 | 0 |
| $S_{785}$ | 18.0 | 0.7 | 18.9 | 17.7 | 17.5 | 17.3 | 18.5 |
| Scaling | 0.57 | 0.13 | 0.64 | 0.66 | 0.38 | 0.66 | 0.47 |

TABLE III. Model 2: Results of the fit for each ND accounting only spin-independent ionization and recombination. An asterisk indicates parameters that were fixed for this model.

| | Mean | Standard Deviation | ND1 | ND2 | ND3 | ND4 | ND5 |
|---|---|---|---|---|---|---|---|
| $\Omega_{532}^-$ | 60 | 21 | 77 | 31 | 59 | 51 | 84 |
| $\Gamma_{\text{Mag}}^{\text{SF}}$ | 2.5 | 0.8 | 3.5 | 2.3 | 3.0 | 1.3 | 2.5 |
| $\kappa$ | 1.0 | 0.0 | 1.0 | 1.0 | 1.0 | 1.0 | 1.0 |
| $I_{532}$ | 9.1 | 13 | 0.014 | 24.6 | 21.0 | 0.044 | 0.0003 |
| $I_{785}$ | 14 | 3 | 14 | 15 | 21 | 12 | 14 |
| $\mu$* | – | – | 0.5 | 0.5 | 0.5 | 0.5 | 0.5 |
| $R_{532}$ | 77 | 28 | 96 | 114 | 44 | 58 | 74 |
| $R_{785}$ | 58 | 7 | 60 | 54 | 50 | 66 | 62 |
| $\nu$ | 0.86 | 0.18 | 0.93 | 0.56 | 0.79 | 1.0 | 0.99 |
| $S_{785}$* | – | – | 0 | 0 | 0 | 0 | 0 |
| Scaling | 0.16 | 0.15 | 0.08 | 0.04 | 0.36 | 0.03 | 0.27 |

### 1. Model 1

This model only accounts for the stimulated emission process to reproduce the fluorescence quenching, see Table II. In this case, all ionization and recombination rates are set to zero.

### 2. Model 2

This model only accounts for a spin-independent ionization/recombination process to reproduce the fluorescence quenching, see Table III. In this case, the stimulated emission rate is set to zero and the spin selectivity coefficient $\mu$ to 0.5.

TABLE IV. Model 3: Results of the fit for each ND accounting for spin-independent ionization and recombination including stimulated emission. An asterisk indicates parameters that were fixed for this model.

| | Mean | Standard Deviation | ND1 | ND2 | ND3 | ND4 | ND5 |
|---|---|---|---|---|---|---|---|
| $\Omega_{532}^-$ | 78 | 42 | 93 | 26 | 139 | 60 | 72 |
| $\Gamma_{\text{Mag}}^{\text{SF}}$ | 3.7 | 1.8 | 5.5 | 5.3 | 4.0 | 1.5 | 2.0 |
| $\kappa$ | 0.93 | 0.10 | 0.85 | 0.99 | 1.0 | 0.99 | 0.79 |
| $I_{532}$ | 8.4 | 15.7 | 3.0 | 36.4 | 1.7 | 0.7 | 0.002 |
| $I_{785}$ | 6.3 | 4.5 | 3.1 | 7.5 | 6.3 | 1.5 | 13.1 |
| $\mu$* | – | – | 0.5 | 0.5 | 0.5 | 0.5 | 0.5 |
| $R_{532}$ | 22 | 27 | 3.4 | 50 | 0.7 | 2.6 | 54 |
| $R_{785}$ | 2.1 | 2.6 | 0.7 | 2.3 | 0.3 | 0.6 | 6.4 |
| $\nu$ | 0.40 | 0.45 | 0.000 | 0.002 | 0.24 | 0.98 | 0.76 |
| $S_{785}$ | 76 | 101 | 57 | 28 | 254 | 30 | 10 |
| Scaling | 0.13 | 0.11 | 0.08 | 0.05 | 0.18 | 0.03 | 0.30 |

TABLE V. Model 4: Results of the fit for each ND accounting only for spin-dependent ionization and recombination. An asterisk indicates parameters that were fixed for this model.

| | Mean | Standard Deviation | ND1 | ND2 | ND3 | ND4 | ND5 |
|---|---|---|---|---|---|---|---|
| $\Omega^{-}_{532}$ | 28 | 0.8 | 40 | 28 | 22 | 1.9 | 2.9 |
| $\Gamma^{SF}_{Mag}$ | 6.2 | 3.7 | 6.1 | 2.4 | 9.6 | 2.6 | 10.4 |
| $\kappa$ | 0.70 | 0.23 | 0.80 | 0.32 | 0.77 | 0.96 | 0.65 |
| $I_{532}$ | 14.3 | 6.3 | 12.5 | 4.4 | 20.1 | 15.5 | 19.4 |
| $I_{785}$ | 9.40 | 0.50 | 9.72 | 9.59 | 8.90 | 8.83 | 9.95 |
| $\mu$ | 0.837 | 0.005 | 0.835 | 0.841 | 0.843 | 0.836 | 0.832 |
| $R_{532}$ | 182 | 91 | 116 | 337 | 173 | 135 | 171 |
| $R_{785}$ | 18.8 | 1.8 | 19.5 | 17.3 | 17.7 | 18.0 | 21.8 |
| $\nu$ | 0.49 | 0.06 | 0.44 | 0.59 | 0.51 | 0.46 | 0.45 |
| $S_{785}$* | – | – | 0 | 0 | 0 | 0 | 0 |
| Scaling | 0.37 | 0.38 | 0.16 | 0.04 | 0.83 | 0.08 | 0.73 |

#### 3. Model 3

This model accounts for both a spin-independent ionization/recombination as well as a stimulated emission to reproduce the fluorescence quenching, see Table IV. In this case the spin selectivity coefficient $\mu$ to 0.5.

#### 4. Model 4

This model accounts only for a spin-dependent ionization/recombination process to reproduce the fluorescence quenching, see Table V. In this case the stimulated emission rate is set to zero.

#### 5. Model 5

This model accounts for both a spin-dependent ionization/recombination as well as a stimulated emission to reproduce the fluorescence quenching, see Table VI.

TABLE VI. Model 5: Results of the fit for each ND accounting for spin-dependent ionization and recombination including stimulated emission.

| | Mean | Standard Deviation | ND1 | ND2 | ND3 | ND4 | ND5 |
|---|---|---|---|---|---|---|---|
| $\Omega^{-}_{532}$ | 28 | 0.8 | 40 | 28 | 23 | 1.9 | 3.0 |
| $\Gamma^{SF}_{Mag}$ | 6.1 | 3.6 | 5.9 | 2.4 | 9.1 | 2.6 | 10.2 |
| $\kappa$ | 0.68 | 0.23 | 0.77 | 0.33 | 0.74 | 0.97 | 0.64 |
| $I_{532}$ | 14.2 | 6.2 | 12.0 | 4.6 | 19.7 | 15.5 | 19.1 |
| $I_{785}$ | 9.31 | 0.51 | 9.51 | 9.59 | 8.74 | 8.81 | 9.89 |
| $\mu$ | 0.842 | 0.007 | 0.844 | 0.840 | 0.854 | 0.836 | 0.836 |
| $R_{532}$ | 181 | 93 | 114 | 340 | 167 | 115 | 168 |
| $R_{785}$ | 18.7 | 1.9 | 19.3 | 17.1 | 17.4 | 18.1 | 21.7 |
| $\nu$ | 0.50 | 0.06 | 0.45 | 0.59 | 0.53 | 0.46 | 0.46 |
| $S_{785}$ | 0.25 | 0.24 | 0.52 | 0.01 | 0.48 | 0.03 | 0.20 |
| Scaling | 0.37 | 0.38 | 0.16 | 0.04 | 0.82 | 0.08 | 0.72 |

TABLE VII. Residuals sum of squares of the fits for the different models.

| | Mean | Standard Deviation | ND1 | ND2 | ND3 | ND4 | ND5 |
|---|---|---|---|---|---|---|---|
| Model 1 | 0.403 | 0.032 | 0.386 | 0.357 | 0.416 | 0.441 | 0.414 |
| Model 2 | 0.189 | 0.066 | 0.183 | 0.091 | 0.222 | 0.269 | 0.181 |
| Model 3 | 0.136 | 0.051 | 0.139 | 0.068 | 0.106 | 0.195 | 0.172 |
| Model 4 | 0.113 | 0.049 | 0.129 | 0.054 | 0.076 | 0.178 | 0.130 |
| Model 5 | 0.113 | 0.049 | 0.129 | 0.054 | 0.076 | 0.178 | 0.130 |

## APPENDIX D: COMPARING MODELS

The residuals for each model and nanodiamond can be observed in Table VII.

In order to compare models with differing numbers of free parameters (5, 9, 10, 10, and 11 for models 1, 2, 3, 4, and 5, respectively) we used the Akaike information criterion.

#### Akaike information criterion

The Akaike information criterion (AIC) estimates the relative quality of a model by measuring the goodness of fit and applying a penalty to models with a higher number of free parameters. The penalty discourages overfitting because the increasing number of parameters in a model almost always improves the goodness of fit. The model provides a likelihood function for the model that is dependent on the sample size $n$, the number of parameters $k$, and the residual sum of squares of the fit from regression (RSS). We first start with determining the AIC value of each model, given by

$$\mathrm{AIC} = n \ln(\mathrm{RSS}/n) + 2k + \frac{2k(k+1)}{n-k-1}. \tag{D1}$$

It is then interesting to compare the different models to the best model that is defined as the model providing the smallest AIC value. The relative AIC of the $i$th model to the best model is then given by

$$\Delta_i = \mathrm{AIC}_i - \min(\mathrm{AIC}). \tag{D2}$$

The relative likelihood $\mathcal{L}$ of the model given the data is then given by

$$\mathcal{L}_i = \exp\left(-\frac{\Delta_i}{2}\right) \tag{D3}$$

In order to better interpret this value we can normalize these relative likelihood values across all the models to give the Akaike weights,

$$w_i = \frac{\mathcal{L}_i}{\sum_{j=1}^{5} \mathcal{L}_j}. \tag{D4}$$

The Akaike weights can now be interpreted as the probability that the model $i$ is the best model given the data and the set of candidate models.

TABLE VIII. Analysis of the different models using the AIC; $k$ is the number of free parameters, $\Delta_i$ is the AIC, and $w_i$ are the Akaike weights.

| | $k$ | Mean RSS | $\Delta_i$ | $w_i$ |
|---|---|---|---|---|
| Model 4 | 10 | 0.113 | 0 | 0.753 |
| Model 5 | 11 | 0.113 | 2.2 | 0.247 |
| Model 3 | 10 | 0.136 | 40.2 | 0.000 |
| Model 2 | 9 | 0.189 | 105.0 | 0.000 |
| Model 1 | 5 | 0.403 | 259.1 | 0.000 |

For our five models the Akaike information criterion analysis is summarized in Table VIII.

As a result of the Akaike information criterion analysis, we have concluded that model 4 is 3 times more likely than model 5 and can exclude the remaining models. While model 4 is the most likely model and the one discussed in the main body of the paper, this is true only for steady-state conditions. The implication is that the stimulated emission pathway has a small impact on the steady-state populations. Under nonsteady-state pulsed regimes the stimulated emission pathway may still have a significant impact on the transient populations of the NV center.


[1] G. Davies and M. F. Hamer, Proc. R. Soc. London, Ser. A **348**, 285 (1976).

[2] P. Siyushev, H. Pinto, M. Vörös, A. Gali, F. Jelezko, and J. Wrachtrup, Phys. Rev. Lett. **110**, 167402 (2013).

[3] M. W. Doherty, N. B. Manson, P. Delaney, F. Jelezko, J. Wrachtrup, and C. L. Hollenberg, Phys. Rep. **528**, 1 (2013).

[4] S. Arroyo-Camejo, M.-P. Adam, M. Besbes, J.-P. Hugonin, V. Jacques, J.-J. Greffet, J.-F. Roch, S. W. Hell, and F. Treussart, ACS Nano **7**, 10912 (2013).

[5] L. P. McGuinness, Y. Yan, A. Stacey, D. A. Simpson, L. T. Hall, D. Maclaurin, S. Prawer, P. Mulvaney, J. Wrachtrup, F. Caruso, R. E. Scholten, and L. C. L. Hollenberg, Nat. Nanotechnol. **6**, 358 (2011).

[6] P. Neumann, N. Mizuochi, F. Rempp, P. Hemmer, H. Watanabe, S. Yamasaki, V. Jacques, T. Gaebel, F. Jelezko, and J. Wrachtrup, Science **320**, 1326 (2008).

[7] E. Togan, Y. Chu, A. S. Trifonov, L. Jiang, J. Maze, L. Childress, M. V. G. Dutt, A. S. Sørensen, P. R. Hemmer, A. S. Zibrov, and M. D. Lukin, Nature (London) **466**, 730 (2010).

[8] P. Neumann, R. Kolesov, B. Naydenov, J. Beck, F. Rempp, M. Steiner, V. Jacques, G. Balasubramanian, M. L. Markham, D. J. Twitchen, S. Pezzagna, J. Meijer, J. Twamley, F. Jelezko, and J. Wrachtrup, Nat. Phys. **6**, 249 (2010).

[9] C. L. Degen, Appl. Phys. Lett. **92**, 243111 (2008).

[10] G. Balasubramanian, I. Y. Chan, R. Kolesov, M. Al-Hmoud, J. Tisler, C. Shin, C. Kim, A. Wojcik, P. R. Hemmer, A. Krueger, T. Hanke, A. Leitenstorfer, R. Bratschitsch, F. Jelezko, and J. Wrachtrup, Nature (London) **455**, 648 (2008).

[11] J. M. Taylor, P. Cappellaro, L. Childress, L. Jiang, D. Budker, P. R. Hemmer, A. Yacoby, R. Walsworth, and M. D. Lukin, Nat. Phys. **4**, 810 (2008).

[12] F. Jelezko and J. Wrachtrup, Phys. Status Solidi A **203**, 3207 (2006).

[13] N. Aslam, G. Waldherr, P. Neumann, F. Jelezko, and J. Wrachtrup, New J. Phys. **15**, 013064 (2013).

[14] R. Schirhagl, K. Chang, M. Loretz, and C. L. Degen, Annu. Rev. Phys. Chem. **65**, 83 (2014).

[15] T. Plakhotnik and R. Chapman, New J. Phys. **13**, 045001 (2011).

[16] R. Chapman and T. Plakhotnik, Phys. Rev. B **86**, 045204 (2012).

[17] N. D. Lai, O. Faklaris, D. Zheng, V. Jacques, H.-C. Chang, J.-F. Roch, and F. Treussart, New J. Phys. **15**, 033030 (2013).

[18] M. Geiselmann, R. Marty, F. J. García de Abajo, and R. Quidant, Nat. Phys. **9**, 785 (2013).

[19] M. L. Juan, C. Bradac, B. Besga, M. Johnsson, G. Brennen, G. Molina-Terriza, and T. Volz, Nat. Phys. **13**, 241 (2016).

[20] O. Romero-Isart, M. L. Juan, R. Quidant, and J. I. Cirac, New J. Phys. **12**, 033015 (2010).

[21] D. E. Chang, C. A. Regal, S. B. Papp, D. J. Wilson, J. Ye, O. Painter, H. J. Kimble, and P. Zoller, Proc. Natl. Acad. Sci. USA **107**, 1005 (2010).

[22] C.-C. Fu, H.-Y. Lee, K. Chen, T.-S. Lim, H.-Y. Wu, P.-K. Lin, P.-K. Wei, P.-H. Tsao, H.-C. Chang, and W. Fann, Proc. Natl. Acad. Sci. USA **104**, 727 (2007).

[23] R. McMurtrie, L. J. Rogers, and N. B. Manson, Phys. Procedia **3**, 1583 (2010).

[24] K. Burnham and D. Anderson, *Model Selection and Multimodel Inference: A Practical Information-Theoretic Approach* (Springer, New York, 1993).

[25] B. Prasanna Venkatesh, M. L. Juan, and O. Romero-Isart, Phys. Rev. Lett. **120**, 033602 (2018).

[26] J. Storteboom, P. Dolan, S. Castelletto, X. Li, and M. Gu, Opt. Express **23**, 11327 (2015).

[27] F. A. Inam, T. Gaebel, C. Bradac, L. Stewart, M. J. Withford, J. M. Dawes, J. R. Rabeau, and M. J. Steel, New J. Phys. **13**, 073012 (2011).

[28] V. M. Acosta, A. Jarmola, E. Bauch, and D. Budker, Phys. Rev. B **82**, 201202(R) (2010).

[29] L. Robledo, H. Bernien, T. van der Sar, and R. Hanson, New J. Phys. **13**, 025013 (2011).

[30] M. L. Goldman, A. Sipahigil, M. W. Doherty, N. Y. Yao, S. D. Bennett, M. Markham, D. J. Twitchen, N. B. Manson, A. Kubanek, and M. D. Lukin, Phys. Rev. Lett. **114**, 145502 (2015).

[31] M. L. Goldman, M. W. Doherty, A. Sipahigil, N. Y. Yao, S. D. Bennett, N. B. Manson, A. Kubanek, and M. D. Lukin, Phys. Rev. B **91**, 165201 (2015).

[32] G. Liaugaudas, G. Davies, K. Suhling, R. U. A. Khan, and D. J. F. Evans, J. Phys.: Condens. Matter **24**, 435503 (2012).

[33] M. Berthel, O. Mollet, G. Dantelle, T. Gacoin, S. Huant, and A. Drezet, Phys. Rev. B **91**, 035308 (2015).

[34] A. Jarmola, V. M. Acosta, K. Jensen, S. Chemerisov, and D. Budker, Phys. Rev. Lett. **108**, 197601 (2012).

[35] J.-P. Tetienne, L. Rondin, P. Spinicelli, M. Chipaux, T. Debuisschert, J.-F. Roch, and V. Jacques, New J. Phys. **14**, 103033 (2012).

[36] P. Ji and M. V. Gurudev Dutt, Phys. Rev. B **94**, 024101 (2016).

[37] I. Meirzada, Y. Hovav, S. A. Wolf, and N. Bar-Gill, Phys. Rev. B **98**, 245411 (2018).

[38] X.-D. Chen, S. Li, A. Shen, Y. Dong, C.-H. Dong, G.-C. Guo, and F.-W. Sun, Phys. Rev. Appl. **7**, 014008 (2017).

[39] L. J. Rogers, S. Armstrong, M. J. Sellars, and N. B. Manson, New J. Phys. **10**, 103024 (2008).

[40] N. B. Manson and J. P. Harrison, Diam. Relat. Mater. **14**, 1705 (2005).

[41] S. Felton, A. M. Edmonds, M. E. Newton, P. M. Martineau, D. Fisher, and D. J. Twitchen, Phys. Rev. B **77**, 081201(R) (2008).